PAPER

Pressure-induced stiffness of Au nanoparticles to 71 GPa under quasi-hydrostatic loading

Pressure-induced stiffness of Au nanoparticles to 71 GPa under quasi-hydrostatic loading

Xinguo Hong[1], Thomas S. Duffy[2], Lars Ehm[1,3] and Donald J. Weidner[1]

[1]*Mineral Physics Institute, Stony Brook University, Stony Brook, NY 11794, USA*

[2]*Department of Geosciences, Princeton University, Princeton, NJ 08544, USA*

[3]*Photon Sciences Directorate, Brookhaven National Laboratory, Upton, NY 11973, USA*

ABSTRACT

The compressibility of nanocrystalline gold (n-Au, 20 nm) has been studied by X-ray total scattering using high-energy monochromatic X-rays in the diamond anvil cell (DAC) under quasi-hydrostatic conditions up to 71 GPa. The bulk modulus, K_0, of the n-Au obtained from fitting to a Vinet equation of state is ~196(3) GPa, which is about 17% higher than for the corresponding bulk materials (K_0: 167 GPa). At low pressures (<7 GPa), the compression behavior of n-Au shows little difference from that of bulk Au. With increasing pressure, the compressive behavior of n-Au gradually deviates from the equation of state (EOS) of bulk gold. Analysis of the pair distribution function (PDF), peak broadening and Rietveld refinement reveals that the microstructure of n-Au is nearly a single-grain/domain at ambient conditions, but undergoes substantial pressure-induced reduction in grain size until 10 GPa. The results indicate that the nature of the internal microstructure in n-Au is associated with the observed EOS difference from bulk Au at high pressure. Full-pattern analysis confirms that significant changes in grain size, stacking faults, grain orientation and texture occur in n-Au at high pressure. We have observed direct experimental

evidence of a transition in compressional mechanism for n-Au at ~20 GPa, i.e., fromdeformation dominated by nucleation and motion of lattice dislocations (dislocation-mediated) to a prominent grain boundary mediated response to external pressure. The internal microstructure inside the nanoparticle (nanocrystallinity) plays a critical role for the macro-mechanical properties of nano-Au.

I. Introduction

The optical, electronic, structural and mechanical properties of nanoparticles (1—100 nm) can significantly differ from those of their bulk counterparts due to quantum and structural confinement effects [1-3]. The potential applications of size-tailored mechanical properties in nanoscale materials has driven intensive investigations on their mechanical behavior [1-5]. The mechanical properties of nanoparticles defined by both elastic and plastic properties are fundamental quantities in physics, engineering and geoscience [4-10].

Thus far X-ray diffraction has played a dominant role in exploring the mechanical properties of nanoparticles at high pressure [4,5,7]. Despite extensive studies, the mechanical properties of nanoparticles as a function of their particle size are still not well understood because of inconsistent results on the size-dependence of the bulk modulus. With decreasing particle size, the bulk modulus is reported to be either enhanced (γ -Fe_2O_3 [8], Ge_3N_4 [11], Au[4,5] and Ag [4] [12]), decreased (Cu [13], Pd [14], CdSe [15], ZnS [16], Pt [17] and TiO_2 [18]), or independent of particle size (Fe [19], Ni [20] and TiC [21]). These apparently contradictory findings requires detailed structural information about the internal nano-crystallinity, i.e. the internal structure in nanocrystals, which may affect their chemical and physical properties, but is not well understood [9,22].

Gold is a face-centered-cubic (FCC) metal with low strength that has been thoroughly studied theoretically and experimentally at high pressures [23-34]. Although a hexagonal close-packed structure may be formed at very high pressure and temperature [35], the FCC structure is stable to at least 250 GPa [34]. Gold has a number of attributes that make it useful as a pressure standard in high-pressure experiments including its low strength, moderate compressibility, chemical inertness, and good X-ray scattering power. Many high-pressure experiments [5,6,30-

34,36,37] have been carried out to establish an accurate equation of state (EOS) for Au. A large difference in the EOS between n-Au and its bulk counterpart, as reported in Ref. [4], would rule out n-Au as a pressure calibrant for experiments in the mutli-megabar region using an X-ray nanoprobe as being developed in some 3rd and 4th synchrotron radiation facilities [38].

It is known that there are several experimental factors which may cause discrepancy in EOS parameters obtained from static high-pressure experiments: experimental error, different pressure scales, different EOS formulation, non-hydrostatic stress, and so on [32,34]. The most common source of systematic error stems from non-hydrostatic stresses during compression in the diamond anvil cell (DAC). The presence of non-hydrostatic stresses can bias equations of state considerably [32,39-43]. As a result, EOS parameters determined under non-hydrostatic conditions may be incorrect [36]. In a conventional diamond anvil cell geometry, the non-hydrostatic compression curve can yield a volume that lies as large as much as 10—20 % above the quasi-hydrostatic curve at a given pressure [36]. Truly hydrostatic conditions are only obtained when the sample is contained within a fluid pressure medium in the DAC, but all known pressure media freeze below ~13 GPa at room temperature. As one of the most commonly used pressure transmitting media, methanol–ethanol (4:1) has a hydrostatic limit of 10.5 GPa, and its non-hydrostatic stresses increase rapidly above this pressure [43] making it unsuitable for the EOS determination at pressures significantly above 10 GPa. To minimize the effect of uniaxial stress on the sample volume, we employed solid argon as a pressure medium due to its low strength and chemical inertness [43].

Another key approach for understanding the mechanical properties of nanoparticles is to explore features of the internal nano-crystallinity such as grain size, grain boundaries and texture as a function of pressure [9]. For example, a recent study indicates the internal grain rotation is the

dominant mechanism of plastic deformation in ultrafine nanomaterials [9]. However, the *in situ* observation of grain size, rotation and texture at the nanoscale is much more difficult than for coarse-grained materials [7,9]. Here we examine Au nanocrystals using high-energy X-ray diffraction and employ multiple analysis techniques, including pair distribution function measurements (PDF), peak broadening analysis and Rietveld refinement.

PDF analysis enables characterization of the structural variation of short, intermediate, and long range order in materials. The X-ray diffraction pattern of nanoparticles consists of Bragg-like peaks together with a diffuse component, both of which contribute to the PDF[44]. The atomic PDF obtained by high-energy X-ray or neutron diffraction is a powerful tool for studying nanoparticles [2,44-46].

Application of PDF measurements to samples compressed in the DAC is hindered by limitations in obtaining sufficiently small X-ray beamsizes when using high-energy radiation. In previous work, the PDF of n-Au was measured up to 10 GPa in an alcohol pressure-medium of methanol:ethanol (4:1) using a 50×50 μm unfocused X-ray beam [46]. Acquiring PDFs using such a large unfocused beam for high-pressure DAC experiments is subject to low X-ray intensity, long data collection time, possible parasitic scattering from slits, and relatively large diamond and gasket background contributions. Together all of these factors have restricted PDF analysis to pressures below 10 GPa so far [46,47]. In this work we examine the compressibility of n-Au in the diamond anvil cell under quasi-hydrostatic conditions at pressures up to 71 GPa by using a micro-focused high-energy X-ray beam.

II. Experiment

The sample consisted of spherical Au nanoparticles (99.9%, 10—20 nm mean particle size,

Nanostructured & Amorphous Materials, Inc., USA). High-pressure X-ray total scattering experiments were performed at beamline X17B3 of the National Synchrotron Light Source at Brookhaven National Laboratory.

A high-energy monochromatic X-ray beam was obtained using a sagittally bent double-Laue monochromator, and further focused to a beam size of 15 x 15 μm^2 using Pt coated Kirkpatrick-Baez mirrors. Parasitic scattering from the upstream slits and mirrors were blocked with a clean-up system using a steel tube with a 0.4-mm pinhole in a 5-mm thick Pb disk at one end. The X-ray wavelength was measured to be 0.15231±0.00004 Å (81.400±0.024 keV) [48]. The sample—detector distance and detector orientation were calibrated using a CeO_2 standard.

Piston-cylinder diamond anvil cells with 100-degree conical openings and 300-μm diameter culets were used for pressure generation. The accessible range of measured q-space is up to 20 $Å^{-1}$. The n-Au powder samples were loaded into a 100-μm diameter hole in a rhenium gasket that had been pre-indented to a thickness of 50 μm. Argon was used as pressure-transmitting medium to prevent/minimize deviatoric stress. The sample was loaded as a loose powder to minimize particle contacts that are known to result in development of grain-to-grain microstresses. Ruby chips were placed at the edge of sample chamber for pressure determination using the ruby fluorescence technique [49].

The high-pressure total X-ray scattering data were collected using a Perkin-Elmer flat panel detector (XRD 1261). This large-area detector is optimized for high-energy radiation and facilities collection to a higher Q range but has a high dark current. In order to optimize counting statistics, alternating data and dark current series were collected, typically up to 100-200 datasets. The series of data/dark current spectra were then averaged for dark current reduction in order to improve the statistical accuracy. The program Fit2D [50] was used to process the 2D X-ray diffraction images.

An empty diamond anvil cell at ambient pressure was measured as a reference "background" sample. The diffraction peaks of the diamond anvils and the weak Ar pressure medium were masked prior to the conversion from two-dimensional to one-dimensional diffraction patterns in FIT2D. Samples were compressed to maximum pressures of 46—71 GPa in two independent DAC experiments. Pressure was measured both before and after each PDF measurement and the pressure difference was typically 0.5 GPa or less.

The total scattering function, *S(Q),* and the pair distribution function, *G(r)*, were obtained using the program PDFgetX2 [51]. The high-pressure n-Au data were fitted to the experimentally determined *G(r)* using the program PDFgui [52]. For the same data sets, Rietveld refinements were performed using the Jana2006, a universal program for structure refinement/determination covering standard and advanced crystallography [53]. Full-pattern MAUD (Materials Analysis Using Diffraction) analysis provides additional information about the sample microstructure, such as grain, stress, strain and texture [54].

III. Results and Discussion

3.1) PDF analysis

Figure 1 shows the PDF measurement at ambient pressure for n-Au. The atomic pair distribution function (PDF), *G(r)*, is defined as:

$$G(r) = 4\pi r[\rho(r) - \rho_o], \quad (1)$$

where ρ_0 is the average atomic number density, and $\rho(r)$ is the atomic pair density at a radial distance, r. The function $G(r)$ gives information about the probability of finding neighboring atoms at the distance r from a given atom. Experimentally, $G(r)$ is obtained from the Fourier transformation of the structure function $S(Q)$,

$$G(r) = \frac{\pi}{2}\int_0^\infty Q[S(Q) - 1]\sin(Qr)\,dQ, \qquad (2)$$

where *S(Q)*, the total scattering structure function, is related to the coherent part of the total diffracted intensity of the material:

$$S(Q) = \frac{I^{coh}(Q) - \sum c_i|f_i(Q)|^2}{|\sum c_i f_i(Q)|^2} + 1, \qquad (3)$$

where $I^{coh}(Q)$ is the coherent scattering intensity, and c_i and $f_i(Q)$ are the atomic concentration and X-ray atomic form factor, respectively, for the atomic species of type *i*. The measured X-ray diffraction data were first reduced to *S(Q)* by Eq. (3) and then a Fourier transform was performed to obtain the atomic PDF, *G(r)* using Eq. (2) and PDFgetX2 software [51]. The *G(r)* function contains all the distinct types of interatomic correlations in the material, as indicated in Eq. (3).

Due to the finite crystallite size and disorder inherent in nanoparticles, the *G(r)* function shows attenuation associated with particle size. The size determination of a nanoparticle is important because the mechanical and other physical and chemical properties may be size dependent. The PDF of a spherical nanoparticle of size *D* can be expressed as [55]:

$$G(r,d) = f_e(r,D) * 4\pi r[\rho(r) - \rho_0] = f_e(r,D)G(r), \qquad (4a)$$

$$\mathrm{f_e(r,D)} = \left[1 - \frac{3}{2}\frac{\mathrm{r}}{\mathrm{D}} + \frac{1}{2}\left(\frac{\mathrm{r}}{\mathrm{D}}\right)^3\right]\Theta(D - r) \qquad (4b)$$

where $\mathrm{f_e(r,D)}$ is the damping envelope function [56] and Θ(x) is the Heaviside step function, which is equal to 0 for x<0 and 1 for x>0.

For size determination, we first refine the PDF of the bulk CeO_2 standard using PDFgui [52] to determine the instrument parameters related to broadening, Q_{broad}, and damping, Q_{damp}; The particle diameter can be obtained by fitting the *G(r)* of n-Au, whose oscillations are attenuated by the envelope function (Eq. 4b).

The upper panel (Fig. 1) shows the reduced total scattering function, *F(Q)=Q(S(Q)-1)* for

n-Au at ambient pressure, while the lower panel represents the corresponding PDF fit. Also shown at the bottom of the lower panel is the difference between the calculated and measured PDFs. The average size of the n-Au sample is determined to be 22 nm with a fit residual, R_w, of 0.094, which is in good agreement with the value of 21 nm determined by MAUD analysis via full-profile least-squares modeling discussed below.

The PDF data are fit well at ambient pressure using a simple FCC Au structure model with a small fit residual. This implies that there is no significant structural modification due to the nano-size effect in n-Au compared to the bulk Au. The measured lattice parameters are 4.07628(3) Å and 4.07626(21) Å by PDF and Rietveld refinement, respectively, and are in excellent agreement with 4.076(1) for 30-nm Au [4], but slightly smaller than the bulk Au 4.0787(3) [32].

Fig. 2 shows the typical PDF fit and Rietveld refinements at 2.1 GPa and 71 GPa for n-Au, using PDFgui [52]and Jana2006 [53] software, respectively. Unlike the PDF fitting in real space, the lattice parameter refinements based on the simple FCC model shows an obvious misfit in the intensity ratio of the 111 and 200 reflections, as reported earlier [4]. The high-pressure PDF fit for n-Au at 2.1 GPa using DAC show a good fit with a residual, R_w, of 0.167.

3.2) Equation of state (EOS) of n-Au

The Vinet equation of state [57] is a commonly used form to parameterize the experimental and theoretical equations of state at high pressure:

$$P = 3K_0\left(\left(\frac{V_0}{V}\right)^{2/3} - \left(\frac{V_0}{V}\right)^{1/3}\right) exp\left[\frac{3}{2}(K_0' - 1)\left(1 - \left(\frac{V_0}{V}\right)^{-1/3}\right)\right], \qquad (5)$$

where P is pressure, and V_0, K_0, and K_0' are the ambient-pressure volume, isothermal bulk modulus and pressure-derivative of K_0, respectively.

The Vinet equation was used to fit the combined pressure-volume data of run-1 and run-2

via non-linear least squares. Figure 3 compares the pressure-volume dependence of n-Au from PDF data with previously reported data of 30nm [4], 50—100 nm [46] and bulk Au [31,34]. The inset shows an expanded view of the region at low pressure. EOS fits were performed by fixing V_0 to the bulk value (67.85 Å^3) but leaving K_0 and K_0' for n-Au free during the fitting. The bulk modulus, K_0, and its pressure-derivative, K_0', of n-Au (20 nm) from our Vinet EOS fit are ~196(3) GPa and 5.7(2), respectively. The bulk modulus, K_0, is about 17% larger than for the corresponding microcrystalline bulk materials (K_0: 167 GPa) [27-30]. Rietveld refinements show a similar EOS with K_0= 198(4) and K_0' =6.3(2). This stands in contrast to the previously reported significantly high stiffness (K_0=286 GPa) for 30 nm n-Au [4]. The bulk modulus, K_0, of n-Au is similar to the previous PDF result for 50-100 nm size n-Au [46], but is much smaller than the reported value for 30-nm Au [4] (inset of Fig. 3). The bulk modulus, K_0, for n-Au is considerably larger than that of bulk Au, whose K_0 = 167 GPa is well-defined by extensive ultrasonic [27-30]and X-ray diffraction (XRD) experiments [25,31,32,34].

The inset of Fig.3 shows the pressure-volume data in the low-pressure range. Our data show good consistency with a previous PDF measurement using alcohol pressure-medium below 7 GPa [46]. The results of Ref. [4] for 30-nm Au and [46] for 0—100 nm Au show large differences in this range despite both using the same methanol–ethanol (4:1) pressure medium. The results of ref. [46] begin to diverge from our data above 7 GPa. It is known that the pressure across the sample volume may be inhomogeneous and differential stress and shear stresses appear at pressures above the freezing of the pressure-transmitting fluid [43]. These stresses can result in decrease in the quality and accuracy of the data [43], and in the appearance of 'anomalies', but might be wrongly ascribed to new physical phenomena. However, since the measured lattice parameters deviate under different stress states, the non-hydrostatic stress cannot be excluded as a

likely cause of the disagreement in the EOS parameters for the difference between n-Au and coarse grain bulk Au. Our data obtained using Ar pressure medium indicates that nano-Au has high stiffness relative to the bulk material, but this stiffening is much lower than reported in earlier work [4] (Fig. 3).

3.3 Grain size determination

Figure 4 shows the pair distribution function, *G(r)*, at high pressures of 2, 20, 39, 71 GPa and the quenched sample (inside the diamond anvil cell). It can be seen that the *G(r)* peak intensities at high correlation distances diminish more rapidly with increasing pressure. The *G(r)* oscillation is reduced at 20 and 39 GPa at r_{max} above 30 Å, but it is recovered upon quenching. The lower panel of Fig. 4 shows the evolution of the average grain or domain size of n-Au determined as a function of pressure from the fits using Eq. 4.

The grain size of n-Au decreases below 10 GPa at a rate which is much higher than that expected due to the effect of compression alone (top red line, Fig. 4b). This indicates the sample have been broken into smaller grains. The variation of grain size is largely reversible upon quench, as reported in an earlier study on nanocrystalline Au [5]. Structural disorder in n-Au arises from two sources. One is due to the larger ratio of grain boundary to volume in nanoparticles which increases further at high pressure. The other is the pressure-induced strain within the nanoparticle that causes correlated shifts in the equilibrium positions relative to the ideal Au lattice. This effect is cumulative and causes the loss of intensity in g(r) with increasing interatomic distance as the case of ZnS [2] and eventually the complete loss of intensity at a correlation length of about 30 Å (Fig. 4a).

As shown in Fig. 3a, at low pressures (<7 GPa), the compression behavior of n-Au is nearly

the same as that of corresponding bulk material. As pressure increases, the EOS of n-Au gradually deviates from the bulk towards relatively larger volumes, reflecting increased lattice stiffness upon compression. There are several causes which may be responsible for the observed lattice stiffening. For example, dislocations at the increased grain boundary within the nanoparticles can lead to a larger distribution of bond lengths and enhances the stiffness [2]. The grain-size related structural disorder in the grain boundary known as the Hall–Petch effect can also be responsible for lattice stiffening. In addition, the strength of n-Au (30 nm) is considerably higher than that of bulk Au [5]. This enhanced strength for small n-Au particles should also contribute the stiffness of n-Au at high pressure.

3.4) Peak width analysis

It is useful to employ complementary techniques that can probe different aspects of the nanoparticle behavior [55]. To cross check the pressure-induced grain size evolution, we have conducted diffraction peak width analysis. Diffraction peak widths increase with pressure due to a number of factors including change in grain size, increasing microstrain, and stress gradients across the sample. The lattice spacing of the Au 111 reflection is known to be the one least affected by the uniaxial stress [32]. Fig. 5a shows the diffraction peak widths (full width at half maximum, FWHM) measured for Au (111) for the two different runs. The peak width of run-1 agrees well with that of run-2.

The particle sizes can be estimated from the Scherrer equation [58,59],

$$W(2\theta) = \frac{K\lambda}{D\cos\theta} \qquad (6)$$

Where $W(2\theta)$ is the peak width, λ is the wavelength, and D is the crystallite size. The constant K is typically close to unity and ranges from 0.8 to 1.39. For FWHM of spherical crystals with cubic

symmetry, K is equal to 0.94 [59]. The Au (111) diffraction peak is the lowest angle peak, and at these high energies, we can approximate $\cos\theta \approx 1$. We take the relative variation of grain size normalized to the width measured at ambient pressure, as below:

$$\frac{D}{D_0} = \frac{W_0(Au111)}{W(Au111)}, \quad (7)$$

where W and W_0 are the FWHM of Au (111) measured at high pressure and ambient pressure, respectively. The obtained data for grain size evolution is plotted at Fig. 5b.

At low pressure (<10 GPa) the grain size decreases rapidly, consistent with the PDF analysis (Fig. 4b). The width of Au (111) peak shows a plateau at 10—30 GPa, followed by more rapid change until 45 GPa before flattening again until 71 GPa. The trend for the grain size evolution between the PDF and peak width analysis at 10—71 GPa is generally similar but not completely consistent. With increasing pressure, diffraction peaks become broader due to several factors including differential stress, strain variation and grain size reduction, and it is difficult to separate the effects of each of these factors. Although solid argon as a pressure medium can provide a good "quasi-hydrostatic" environment, truly hydrostatic conditions cannot be achieved above the solidification pressure of 1.4 GPa. At higher pressures, there remains some deviatoric stress [43], which might drive a reduction in grain size.

3.5 MAUD analysis

Full-pattern refinement using the MAUD software can provide comprehensive information about the sample microstructure, such as grain size, stress, strain and texture [54]. The X-ray diffraction patterns were integrated using FIT2D [13] at azimuthal intervals of 5° over a range of azimuthal angles from δ =0-360°. Our analysis using the MAUD software followed the procedure outlined in Ref. [60]. In brief, the instrumental parameters are adjusted first by refining a standard, e.g. CeO_2 powder. For a proper calibration it is important to use a standard with well-defined lattice

parameters, crystal structure and crystallite size. The standard is used to refine the detector distance, image center and instrumental aberration (Caglioti function) [60]. Next we adjust the background lattice parameters to obtain an approximate solution, and then refine the lattice parameters, structure, and grain size. Finally, we refine all parameters and the texture simultaneously. The E-WIMV method is preferred for quantitative texture analysis [60].

The crystallite size (or average coherent diffraction length, <D>) and root-mean-square microstrains (or atomic level deformations, $<\varepsilon^2>^{1/2}$) were calculated using an isotropic size-strain model. The "Warren" model was used to estimate the stacking fault probability. Figure 6 shows the evolutions of microstrain and twin-fault probabilities as a function of pressure from the Maud analysis.

As shown in Fig.6a, the lattice strain increases strongly with pressure below 10 GPa, followed by a weaker increase to 20 GPa, and then remains near a constant at 20—40 GPa. This is followed by another transition to increased strain (40-60 GPa) and then reduced strain above 60 GPa. This indicates that the n-Au undergoes two changes in deformation behavior occurring at 10—20 GPa and 50—60 GPa, respectively.

Figure 6b shows the obtained twin-fault probabilities. The most striking observation is that there a turning point at 17.5—20 GPa in the twin-fault probability, which should be related to the strain peak near 20 GPa (Fig. 6a). Planar stacking faults are a common defect in crystals which can influence materials properties [61]. The change in behavior near 20 GPa indicates there are two different compression mechanisms in n-Au. Below 20 GPa, there is an increase in stacking faults accompanied by substantial grain size reduction (Fig. 4 and Fig. 5),

The region of steep increase of stacking faults indicates the plastic behavior of n-Au is mainly controlled by the nucleation and motion of lattice dislocations at low pressures (<20 GPa).

A gradual slope means that the nucleation and motion of lattice dislocations become less important due to the spatial confinement of the nanoparticle, and that grain boundary–mediated processes [62] are the prominent response to external pressure for n-Au.

Although the grain size appears to be basically reversible or largely recovered (at ambient pressure, Fig. 4 and Fig. 5), there are still considerable residual strain and stacking faults for the quenched sample from high pressure. This means the compression of n-Au is not fully reversible at the microstructure level as some dislocation defects remain inside the nanoparticle, in contrast to previous speculation [5]. The trapped dislocations may only exist inside the restored grain, because of reversible or largely recovered size of the nanoparticle. The removal of the external stress can lead to partially reversible reabsorption of the dislocations at the grain boundary.

Figure 7 shows the evolution of the average size of the grains/domains determined from MAUD fits as a function of pressure. It can be seen that the grain sizes in Fig. 4-7 are qualitatively similar but quantitatively rather different, e.g. a minimum in grain size at around 40 GPa (Upper panel, Fig. 7) in contrast to the monotonic reduction in size that saturates rather quickly (Fig. 4b), because current PDFgui analysis [52] and peak width analysis don't include some advanced structural information such as stress, strain and texture (Insert of upper panel, Fig. 7).The inset shows the evolution of the domain/grain orientation of Au nanocrystallinity. We can see a relatively rapid grain-size reduction at pressures below 10 GPa, consistent with the results of PDF (Fig. 4b) and peak broadening (Fig. 5) analyses. Because of the formation of new grains and grain boundaries, the pressure response of n-Au in this pressure range is mainly controlled by the nucleation and motion of lattice dislocations, i.e. similar to the dominant deformation mechanism of coarse-grained metals. Smaller grains, which increase the likelihood of dislocations running into grain boundaries, are very strong dislocation barriers. This dislocation-related hardening

mechanism associated with the formation of small grains is called the Hall–Petch hardening, or grain-boundary strengthening. In general, smaller grain size will make the material harder, which may be the reason of the observed stiffness in n-Au and EOS starting to bias from the bulk Au (Fig. 3a). The remaining deviatoric stress at high pressure [43] would be the driving force, leading to the substantial reduction in the grainsize in n-Au, similar to the non-hydrostatic condition [5].

As pressure increases, the grain size inside n-Au decreases and forms a minimum at ~40 GPa, and then increases slowly with further compression. This slow increase in grain size should reflect a slight ordering process during the additional strain occurring at above 40 GPa in n-Au (Fig. 6a)

We can estimate the the number of grain/domains inside the nanoparticle using volume relation,

$$N = \frac{\frac{4}{3}\pi(D_0/2)^3}{\frac{4}{3}\pi(D/2)^3} \qquad (8)$$

where D and D_0 is the measured gran/domain size and the initial nano-particle size following the EOS rule under compression (red line, lower panel, Fig. 4). Fig. 7b shows the evolution of the number of grain/domains with pressure. At low pressures, n-Au mainly comprises of single grain/domain particles. Before 20 GPa, the grain number increases slowly, but rapid change to a maximum of six at 40 GPa, suggesting an octahedron-like structure with six domains formed at 40 GPa. At higher pressures, the grain number decreases unexpectedly, which may reflect the stability of n-Au with certain grain numbers. Above 55 GPa, it roughly keeps a twin grained structure.

The above investigations reveal that a nearly single-grain/domain microstructure of n-Au at ambient pressure changes to multiply twinned grains above 20 GPa. The material is composed

of particles of twinned grains in the region where the microstrain shows little dependence on the applied external pressure (Fig. 6a). The nanoparticle meso-structure commonly observed in fcc metals can be divided into two categories: single and twinned nanocrystals [17]. Single crystalline structures bounded by low index facets represent simple polyhedra (cube, octahedron) and their truncated modifications, while the twinned nanocrystals rather assume the forms of decahedra or icosahedra [17,63]. It is known that noble metal nanoparticles, such as Ag, Cu, Pd, and Au, at sizes of 10 nm often possess multiply twinned grains that allow them to adopt shapes and atomic structures not existing in bulk materials [63,64]. The properties exhibited by particles with multiply twinned polycrystalline structures are often far different from those of single-crystalline particles or from the bulk [63-65], as the observed distinct stiffness in the EOS of n-Au reveals (Fig. 3).

The nearly single grain microstructure of n-Au at pressure below 10 GPa makes the, size-induced effect on the structure of bulk Au negligible (Fig. 1), and is consistent with the observed similarity of the mechanical properties of microcrystalline and n-Au at low pressures (Fig. 3). The maximum grain number is close to six (Fig. 7b) around 40 GPa. Due to the spatial confinement imposed by the spherical initial particle, each grain would have an environment approaching five-fold coordination formed by neighboring grains. These grain clusters frequently feature five-fold twin junctions which yield structures that are ideally described as decahedron or icosahedron with irregular tetrahedral grains [63,66]. It is reported that icosahedral structures in Ni, Ar, Cu, Au, Pb, and Ag have the general feature that the strain within each tetrahedron is non-uniform giving rise to a convex deformation of the outer facets [67]. Since these structures are intrinsically strained, addition of pressure should alter the relative energetics of strain and surface energies which could have a large impact in the structural behavior of these particles [63]. When the maximum of grain number is reached (35—45 GPa), the grain boundary–mediated processes are the prominent

response to external pressure for n-Au, as supported by the low rate of stacking fault generation above 20 GPa (Fig. 6b). This change in the deformation mode arises from the grain size–dependent competition by nucleation and motion of dislocations [7,62].

The inset of Fig. 7a shows the evolution of textures evaluated for n-Au by refinement with the E-WIMV model in MAUD. With the increase of differential stress for n-Au in the Ar medium, individual grains rotate and deform preferentially on slip planes, leading to texture development. Although the observation of grain rotation during deformation of micrometer-sized crystals is feasible, *in situ* probing of grain rotation of ultrafine nanocrystals is difficult [7,9]. As shown in Fig. 7a, the texture formed in the 20 nm Au sample is a <110> fiber texture typical of FCC metals under compression [68]. Dislocation glide results in crystallite rotations, generating lattice preferred orientation or texture. The anisotropic physical properties of a polycrystalline material are strongly related to the preferred alignment of its crystallites. The observations of pressure-promoted texturing indicate that under external pressures, grain rotation activities exist in n-Au (Fig. 7a). Grain rotation is suggested to be a dominant mechanism of plastic deformation for ultrafine nanomaterials [7,9].

IV. Summary

Using high-energy monochromatic X-ray micron beam, we have studied the compressibility of nano gold (n-Au, 20 nm) by X-ray total scattering and profile refinement in the diamond anvil cell under quasi-hydrostatic conditions up to 71 GPa. The grain size drops rapidly with pressure increasing (<10 GPa), exhibiting a Hall–Petch hardening progress. After compression, the initial single large grain breaks down and forms a few smaller grains. Detailed analysis reveals pressure-induced variation in grain size, orientation and texture formed in n-Au at

high pressure. We have directly observed a transition of compressional mechanism from a dislocation-mediated to a grain boundary-mediated compression in nano gold. The present studies reveal that internal microstructure beneath the surface of nanoparticle, such as the grain size, grain boundary and orientation, plays a critical role for the macro-mechanical properties of nano-Au.

Acknowledgment

We would like to thank S. Merkel (Lille), Z. Zhong (BNL), X.M. Yu, S. Ghose (BNL) and S. Lin for discussion and assistance. L. Assoufid (ANL) and C. Liu (ANL) are acknowledged for their help with the KB mirrors. This research was supported by COMPRES under NSF EAR 11-57758.

Figure Legends

FIGURE 1. Measured pair distribution function (PDF) of n-Au using high-energy X-ray microbeam (wavelength of 0.15231±0.00004 Å or 81.400±0.024 keV). (Upper panel) Reduced total scattering function F(Q) obtained from the nano Au powder at ambient pressure. (Lower panel) Points are the corresponding PDF function G(r) obtained with an upper limit for the Fourier transform of Q_{max} = 20 $Å^{-1}$. Lines are the simulated PDFs for a structure solution of 22 nm n-Au with a fit residual, R_w, of 0.094. The bottom curve is the difference between measured and simulated PDFs with offset for clarity.

FIGURE 2. (upper panel) Rietveld refinements of the diffraction patterns of n-Au at 71 GPa using Jana2006 software [53]. The inset shows an image of the gold samples (dark field) suspended in Ar pressure medium (bright field) illuminated by a green laser used for pressure measurement. (lower panel) High pressure PDF fit for n-Au at 2.1 GPa with a fit residual, R_w, of 0.167.

FIGURE 3. Pressure dependence of the unit cell volume of n-Au compared to previously reported data for 300nm Au (dashed line) [4] and the bulk material (solid line) [34]. Vinet EOS fit is shown for the PDF data of run-1 and run-2. Inset shows an expanded view of the region at low pressure.

FIGURE 4. (Upper panel) Pair distribution function, g(r), at pressures of 2, 20, 39,71 GPa and after quenching (but with sample still in the diamond cell). It should be noted that the g(r) oscillation decrease above r_{max} =30 Å for 20 and 39 GPa, but recover slightly at 71 GPa and fully

recovered upon quenching. (Lower panel) Evolution of the average size of the Au nanodomains determined from fits to ranges of data of the pair distribution function in the FCC Au structure with pressure. Unfilled square and circle indicate data on pressure release.

FIGURE 5. (Right axis) Full width at half maximum (FWHM) of the Au 111 diffraction peak; (Left axis) Percentage of original grain size as a function of pressure based on peak-broadening analysis. Unfilled square and circle indicate data on pressure release.

FIGURE 6. (a) Full-profile refinement for azimuthally (0 to 360°) unrolled diffraction images of n-Au (above: fit, below: binned data). (b) Evolutions of microstrain and (c) twin-fault probabilities refined by MAUD as a function of pressure, showing a turning point at 17.5 GPa and a factor of approximately seven -fold reduction in twin-fault probabilities.

FIGURE 7. (Upper panel) Evolution of the average size of the nano-domains determined from MAUD fits as a function of pressure. The inset shows the evolution of the domain/grain orientation of Au nanocrystallinity. (Lower panel) Evolution of the number of nano-domains with pressure, suggesting an octahedron of six domains formed at 40 GPa.

References

[1] A. P. Alivisatos, Science **271**, 933 (1996).
[2] B. Gilbert, F. Huang, H. Zhang, G. A. Waychunas, and J. F. Banfield, Science **305**, 651 (2004).
[3] S. H. Tolbert and A. P. Alivisatos, Science **265**, 373 (1994).
[4] Q. F. Gu, G. Krauss, W. Steurer, F. Gramm, and A. Cervellino, Physical Review Letters **100**, 045502 (2008).
[5] A. K. Singh, H. P. Liermann, S. K. Saxena, H. K. Mao, and S. U. Devi, Journal of Physics: Condensed Matter **18**, S969 (2006).
[6] T. S. Duffy, G. Shen, J. Shu, H.-K. Mao, R. J. Hemley, and A. K. Singh, Journal of Applied Physics **86**, 6729 (1999).
[7] B. Chen *et al.*, Science **338**, 1448 (2012).
[8] J. Z. Jiang, J. S. Olsen, L. Gerward, and S. Mørup, EPL (Europhysics Letters) **44**, 620 (1998).
[9] B. Chen, K. Lutker, J. Lei, J. Yan, S. Yang, and H.-k. Mao, Proceedings of the National Academy of Sciences **111**, 3350 (2014).
[10] H. Dong, S. M. Dorfman, Y. Chen, H. Wang, J. Wang, J. Qin, D. He, and T. S. Duffy, Journal of Applied Physics **111**, 123514 (2012).
[11] Z. Wang, Y. Zhao, D. Schiferl, J. Qian, R. T. Downs, H.-K. Mao, and T. Sekine, The Journal of Physical Chemistry B **107**, 14151 (2003).
[12] Y. Sun, W. Yang, Y. Ren, L. Wang, and C. Lei, Small **7**, 606 (2011).
[13] J. Z. Jiang, J. S. Olsen, L. Gerward, and S. Mørup, Nanostructured Materials **12**, 847 (1999).
[14] M. Grewer, J. Markmann, R. Karos, W. Arnold, and R. Birringer, Acta Materialia **59**, 1523 (2011).
[15] S. H. Tolbert and A. P. Alivisatos, Annual Review of Physical Chemistry **46**, 595 (1995).
[16] Z. Wang, L. L. Daemen, Y. Zhao, C. S. Zha, R. T. Downs, X. Wang, Z. L. Wang, and R. J. Hemley, Nat Mater **4**, 922 (2005).
[17] A. S. Mikheykin, V. P. Dmitriev, S. V. Chagovets, A. B. Kuriganova, N. V. Smirnova, and I. N. Leontyev, Applied Physics Letters **101**, 173111 (2012).
[18] V. Swamy, A. Y. Kuznetsov, L. S. Dubrovinsky, A. Kurnosov, and V. B. Prakapenka, Physical Review Letters **103**, 075505 (2009).
[19] B. Chen, D. Penwell, M. B. Kruger, A. F. Yue, and B. Fultz, Journal of Applied Physics **89**, 4794 (2001).
[20] S. Rekhi, S. K. Saxena, R. Ahuja, B. Johansson, and J. Hu, J Mater Sci **36**, 4719 (2001).
[21] Q. F. Gu, G. Krauss, F. Gramm, and W. Steurer, Journal of Physics: Condensed Matter **20**, 445226 (2008).
[22] G. V. Hartland, Nat Mater **6**, 716 (2007).
[23] T. Tsuchiya, Journal of Geophysical Research: Solid Earth **108**, 2462 (2003).
[24] P. Souvatzis, A. Delin, and O. Eriksson, Physical Review B **73**, 054110 (2006).
[25] P. I. Dorogokupets and A. R. Oganov, Physical Review B **75**, 024115 (2007).
[26] W. B. Daniels and C. S. Smith, Physical Review **111**, 713 (1958).
[27] Y. Hiki and A. V. Granato, Physical Review **144**, 411 (1966).
[28] B. Golding, S. C. Moss, and B. L. Averbach, Physical Review **158**, 637 (1967).
[29] S. N. Biswas, P. Van 't Klooster, and N. J. Trappeniers, Physica B+C **103**, 235 (1981).

[30] M. Song, A. Yoneda, and E. Ito, CHINESE SCI BULL **52**, 1600 (2007).
[31] Y. Fei, A. Ricolleau, M. Frank, K. Mibe, G. Shen, and V. Prakapenka, Proceedings of the National Academy of Sciences **104**, 9182 (2007).
[32] K. Takemura and A. Dewaele, Physical Review B **78**, 104119 (2008).
[33] M. Yokoo, N. Kawai, K. G. Nakamura, and K.-i. Kondo, Applied Physics Letters **92**, 051901 (2008).
[34] S. M. Dorfman, V. B. Prakapenka, Y. Meng, and T. S. Duffy, Journal of Geophysical Research: Solid Earth **117**, B08210 (2012).
[35] L. Dubrovinsky *et al.*, Physical Review Letters **98**, 045503 (2007).
[36] T. S. Duffy, G. Shen, D. L. Heinz, J. Shu, Y. Ma, H.-K. Mao, R. J. Hemley, and A. K. Singh, Physical Review B **60**, 15063 (1999).
[37] S.-H. Shim, T. S. Duffy, and K. Takemura, Earth and Planetary Science Letters **203**, 729 (2002).
[38] L. Wang *et al.*, Proceedings of the National Academy of Sciences **107**, 6140 (2010).
[39] A. K. Singh and G. C. Kennedy, Journal of Applied Physics **45**, 4686 (1974).
[40] G. L. Kinsland and W. A. Bassett, Journal of Applied Physics **48**, 978 (1977).
[41] T. S. Duffy, R. J. Hemley, and H.-k. Mao, Physical Review Letters **74**, 1371 (1995).
[42] R. J. Angel, M. Bujak, J. Zhao, G. D. Gatta, and S. D. Jacobsen, Journal of Applied Crystallography **40**, 26 (2007).
[43] S. Klotz, J. C. Chervin, P. Munsch, and G. L. Marchand, Journal of Physics D: Applied Physics **42**, 075413 (2009).
[44] S. J. L. Billinge and M. G. Kanatzidis, Chemical Communications, 749 (2004).
[45] S. J. L. Billinge and I. Levin, Science **316**, 561 (2007).
[46] C. D. Martin, S. M. Antao, P. J. Chupas, P. L. Lee, S. D. Shastri, and J. B. Parise, Applied Physics Letters **86** (2005).
[47] L. Ehm, L. A. Borkowski, J. B. Parise, S. Ghose, and Z. Chen, Applied Physics Letters **98** (2011).
[48] X. Hong, Z. Chen, and T. S. Duffy, Review of Scientific Instruments **83** (2012).
[49] H. K. Mao, J. Xu, and P. M. Bell, Journal of Geophysical Research: Solid Earth **91**, 4673 (1986).
[50] A. P. Hammersley, S. O. Svensson, A. Thompson, H. Graafsma, Å. Kvick, and J. P. Moy, Review of Scientific Instruments **66**, 2729 (1995).
[51] X. Qiu, J. W. Thompson, and S. J. L. Billinge, Journal of Applied Crystallography **37**, 678 (2004).
[52] C. L. Farrow, P. Juhas, J. W. Liu, D. Bryndin, E. S. Božin, J. Bloch, P. Th, and S. J. L. Billinge, Journal of Physics: Condensed Matter **19**, 335219 (2007).
[53] V. Petříček, M. Dušek, and L. Palatinus, in *Zeitschrift für Kristallographie - Crystalline Materials*2014), p. 345.
[54] L. Lutterotti, S. Matthies, H.-R. Wenk, A. S. Schultz, and J. W. Richardson, Journal of Applied Physics **81**, 594 (1997).
[55] A. S. Masadeh, E. S. Božin, C. L. Farrow, G. Paglia, P. Juhas, S. J. L. Billinge, A. Karkamkar, and M. G. Kanatzidis, Physical Review B **76**, 115413 (2007).
[56] R. C. Howell, T. Proffen, and S. D. Conradson, Physical Review B **73**, 094107 (2006).
[57] P. Vinet, J. Ferrante, J. R. Smith, and J. H. Rose, Journal of Physics C: Solid State Physics **19**, L467 (1986).
[58] P. Scherrer, Nachrichten von der Gesellschaft der Wissenschaften zu Göttingen,

Mathematisch-Physikalische Klasse **1918**, 98 (1918).
[59] J. I. Langford and A. J. C. Wilson, Journal of Applied Crystallography **11**, 102 (1978).
[60] I. Lonardelli, H.-R. Wenk, L. Lutterotti, and M. Goodwin, Journal of Synchrotron Radiation **12**, 354 (2005).
[61] Paul J. Schields, Nicholas Dunwoody, Marc Mamak, Claire Gendron, and S. Bates, International Centre for Diffraction Data **51**, 162 (2008).
[62] Z. Shan, E. A. Stach, J. M. K. Wiezorek, J. A. Knapp, D. M. Follstaedt, and S. X. Mao, Science **305**, 654 (2004).
[63] K. J. Koski, N. M. Kamp, R. K. Smith, M. Kunz, J. K. Knight, and A. P. Alivisatos, Physical Review B **78**, 165410 (2008).
[64] C. L. Johnson, E. Snoeck, M. Ezcurdia, B. Rodriguez-Gonzalez, I. Pastoriza-Santos, L. M. Liz-Marzan, and M. J. Hytch, Nat Mater **7**, 120 (2008).
[65] A. S. Mikheykin, V. P. Dmitriev, S. V. Chagovets, A. B. Kuriganova, N. V. Smirnova, and I. N. Leontyev, Applied Physics Letters **101** (2012).
[66] L. D. Marks, Reports on Progress in Physics **57**, 603 (1994).
[67] D. Reinhard, B. D. Hall, D. Ugarte, and R. Monot, Physical Review B **55**, 7868 (1997).
[68] U. F. Kocks, C. N. Tomé, and H.-R. Wenk, *Texture and Anisotropy Preferred Orientations in Polycrystals and their Effect on Materials Properties* (Cambridge University Press, 2000).

Figure 1

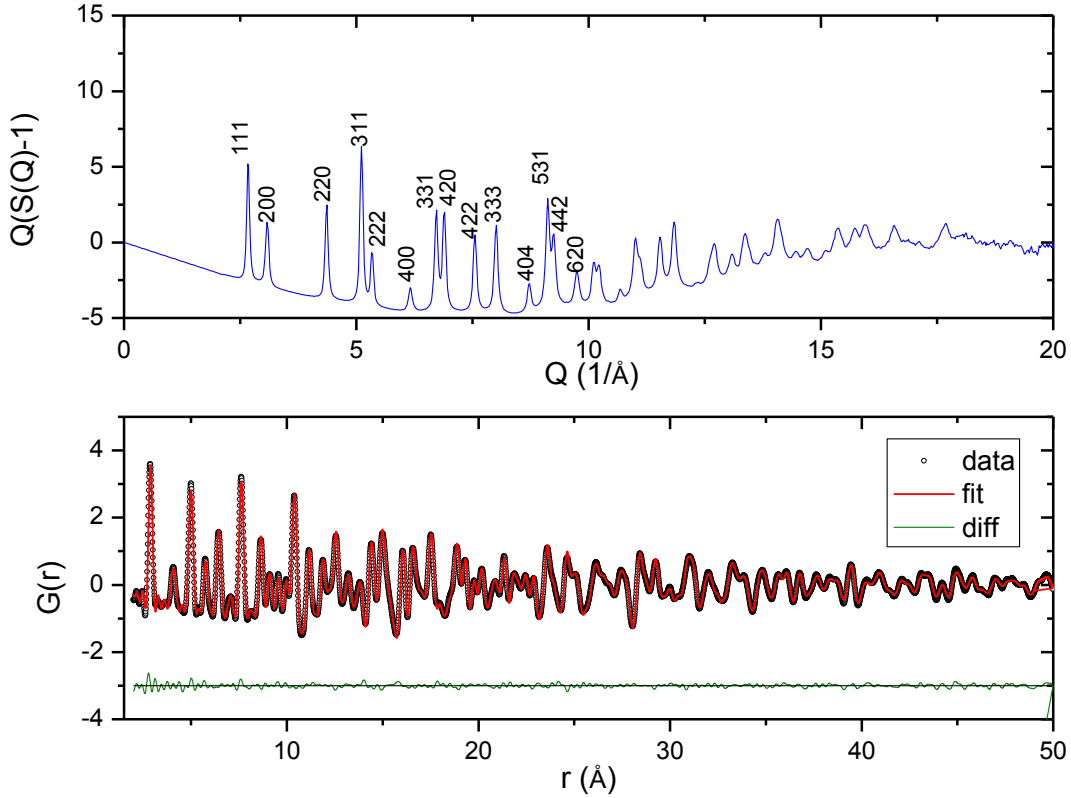
Q(S(Q)-1)
Q (1/Å)
111
200
220
311
222
400
331
420
422
333
404
531
442
620
G(r)
r (Å)
data
fit
diff

Figure 2

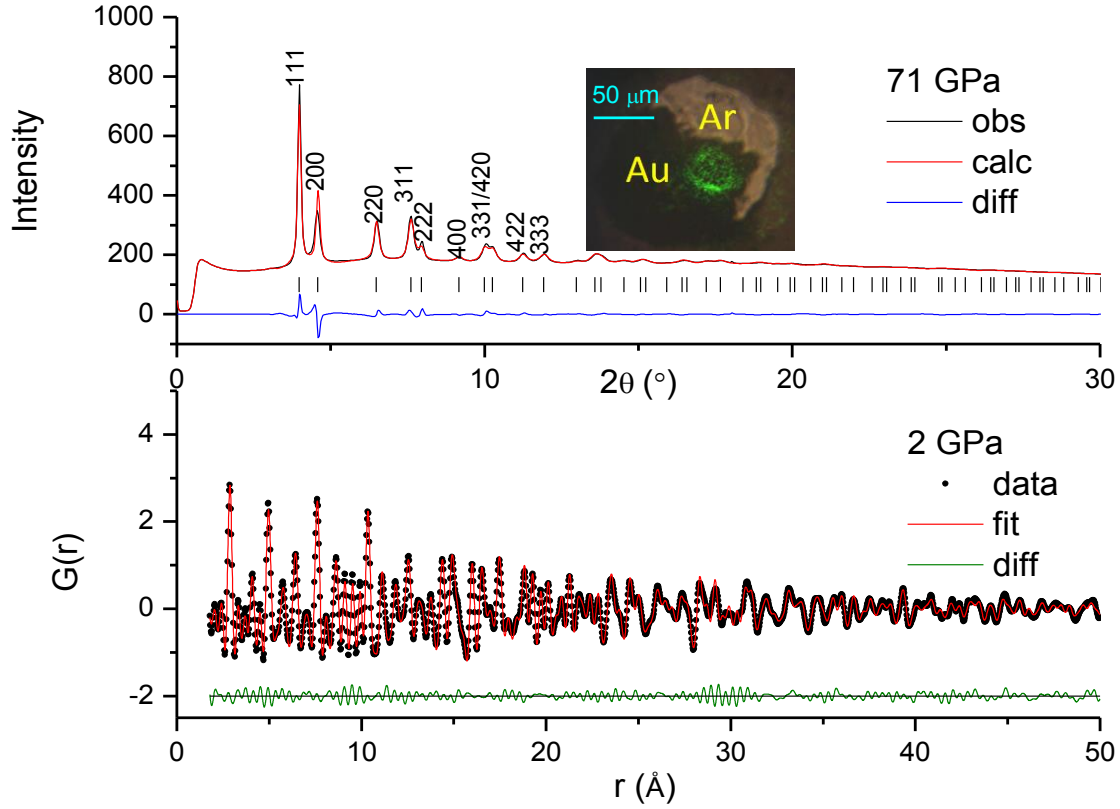
Intensity
1000
800
600
400
200
0
111
200
220
311
222
400
331/420
422
333
50 μm
Ar
Au
71 GPa
obs
calc
diff
0
10
2θ (°)
20
30
G(r)
4
2
0
-2
2 GPa
data
fit
diff
0
10
20
30
40
50
r (Å)

Figure 3

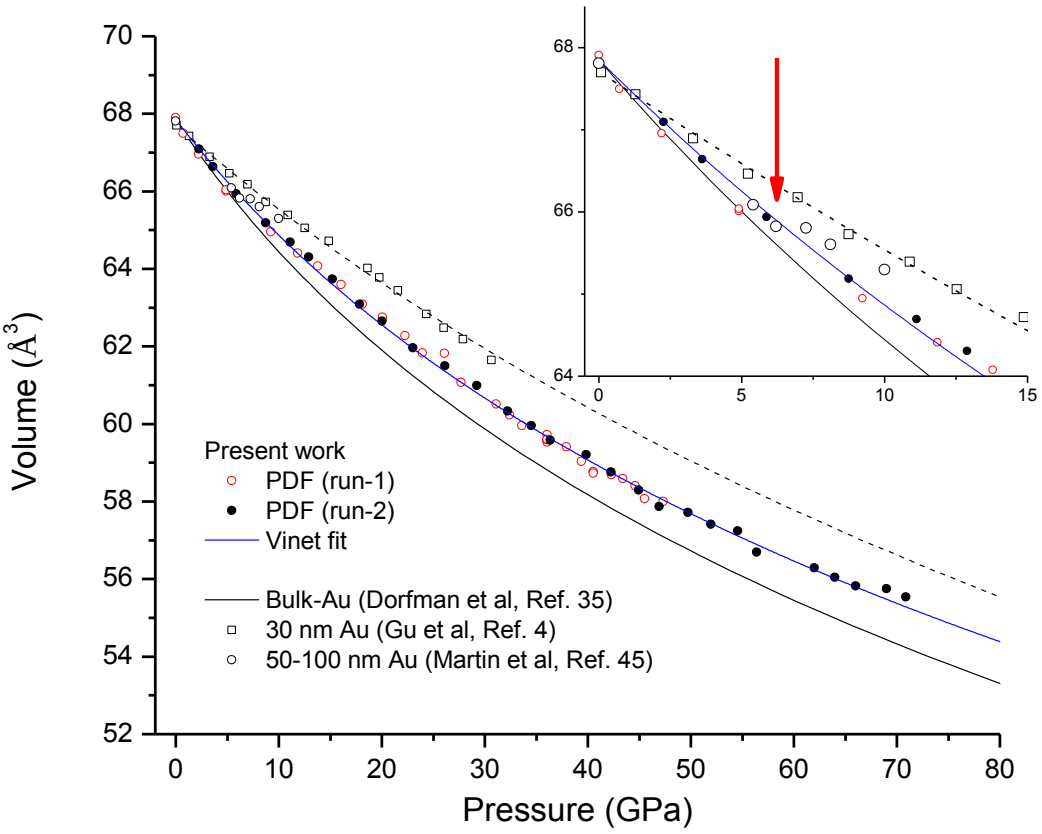
Volume (Å^3)
Pressure (GPa)
Present work
PDF (run-1)
PDF (run-2)
Vinet fit
Bulk-Au (Dorfman et al, Ref. 35)
30 nm Au (Gu et al, Ref. 4)
50-100 nm Au (Martin et al, Ref. 45)

Figure 4

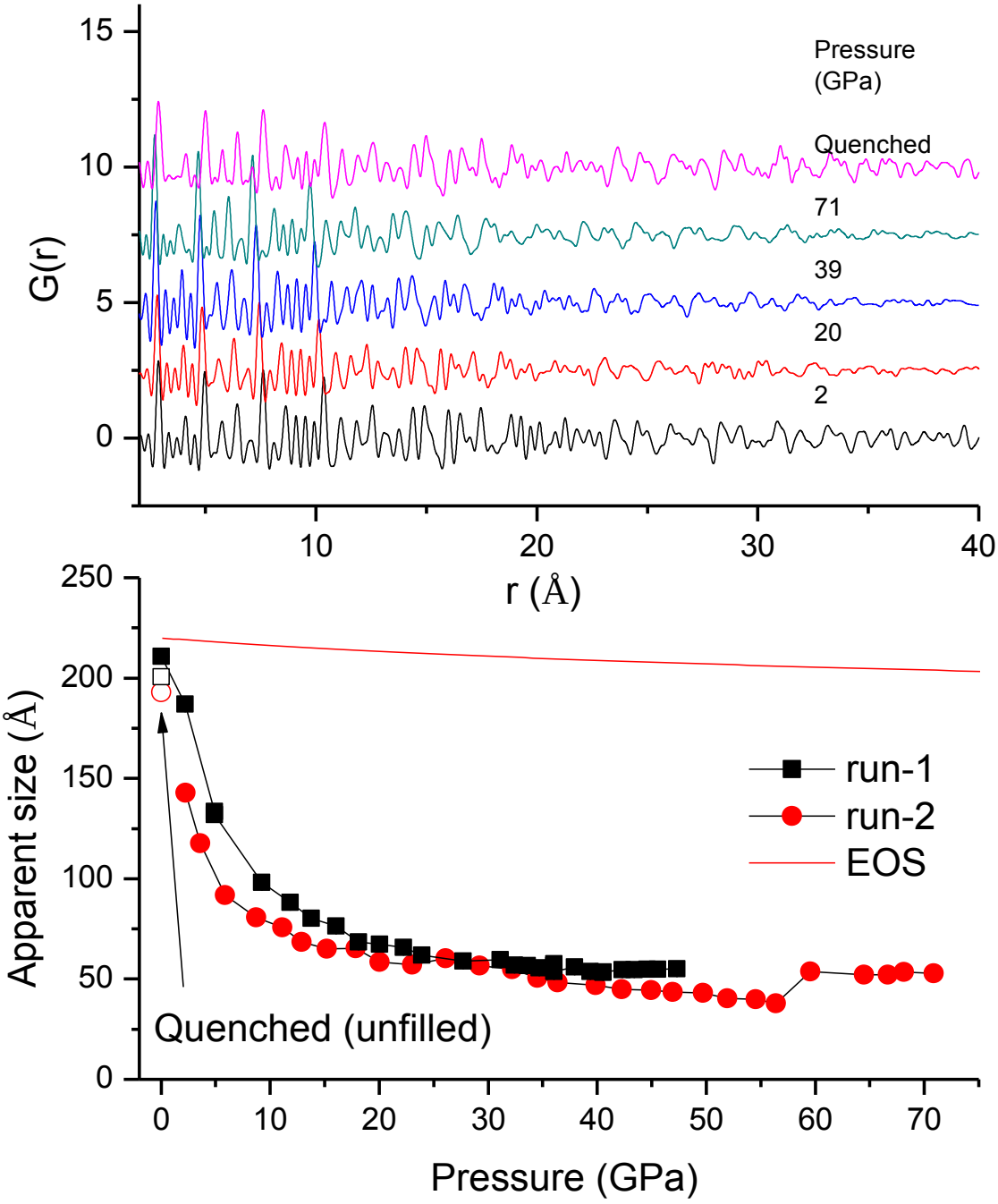
Pressure
(GPa)
Quenched
71
39
20
2
G(r)
r (Å)
Apparent size (Å)
run-1
run-2
EOS
Quenched (unfilled)
Pressure (GPa)

Figure 5

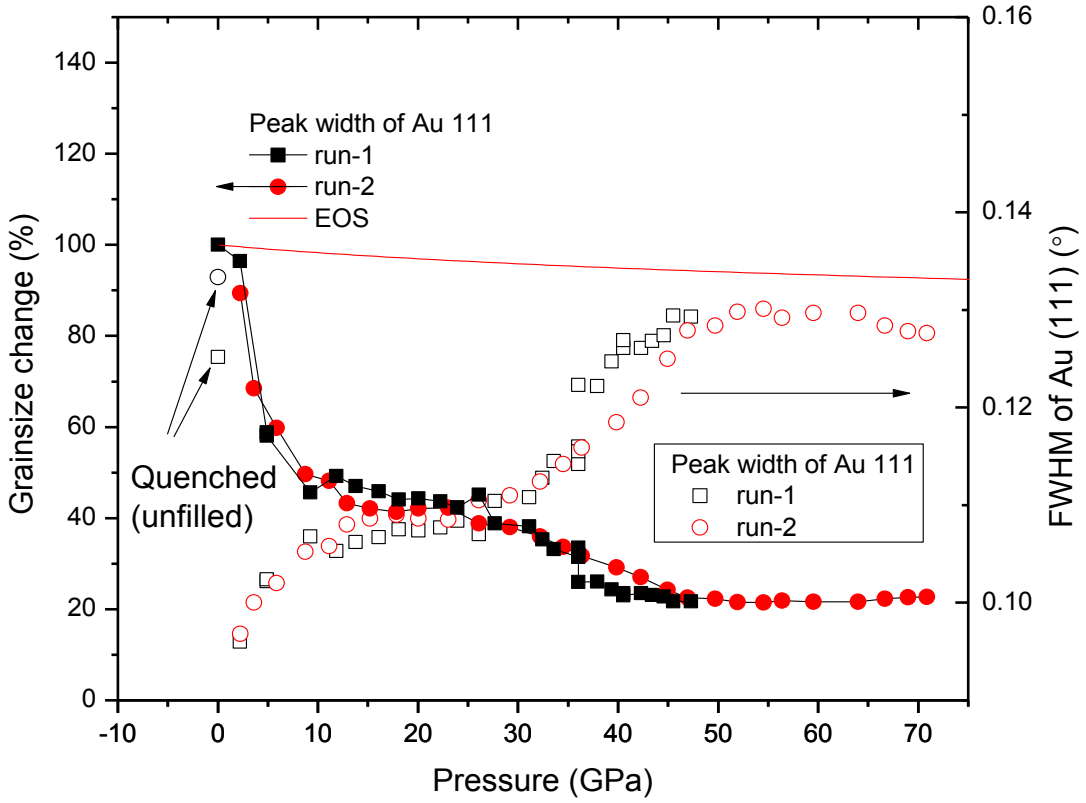
Peak width of Au 111
run-1
run-2
EOS
Quenched
(unfilled)
Peak width of Au 111
run-1
run-2
Grainsize change (%)
FWHM of Au (111) (°)
Pressure (GPa)
0
20
40
60
80
100
120
140
0.10
0.12
0.14
0.16
-10
0
10
20
30
40
50
60
70

Figure 6

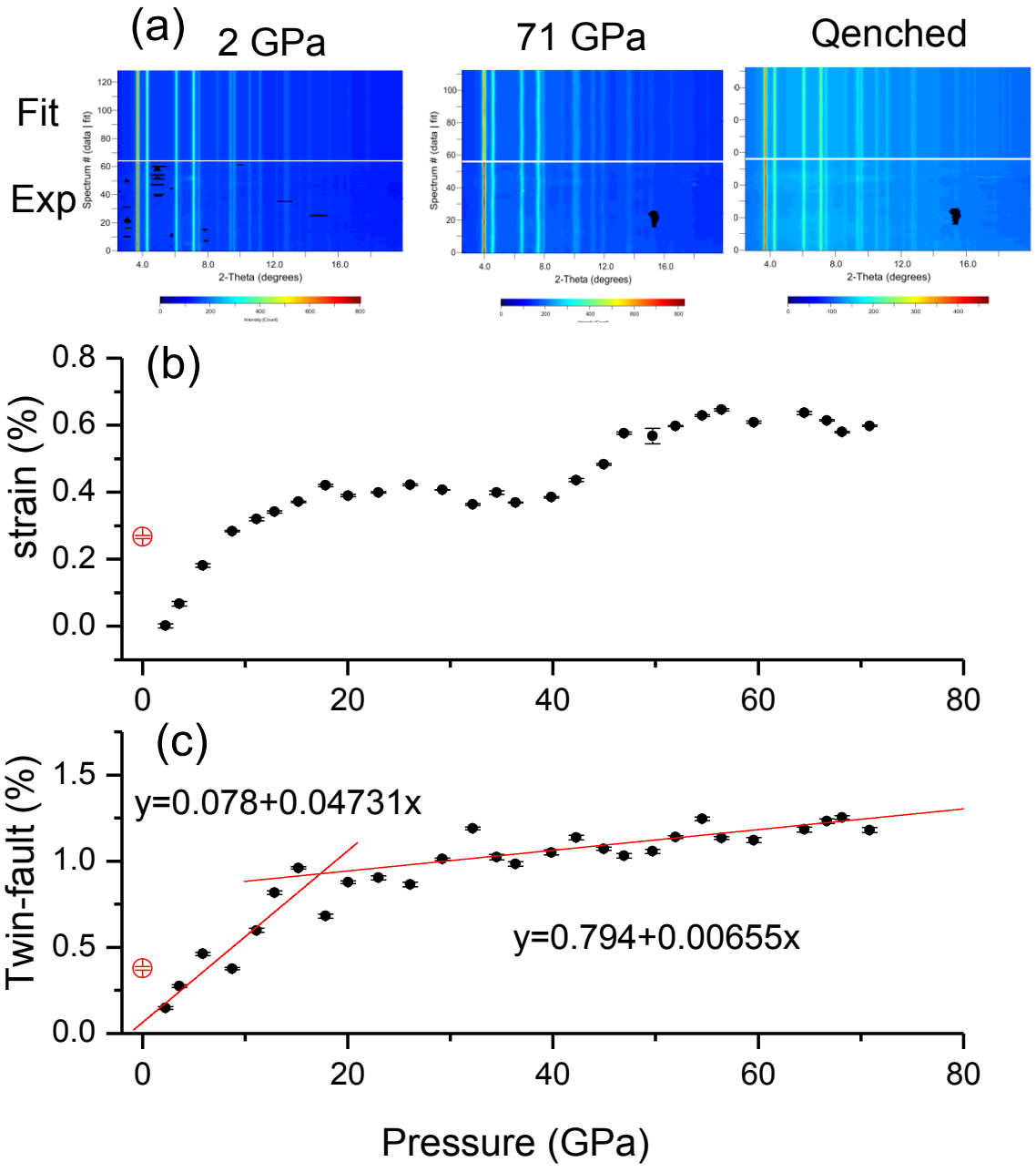
(a)
2 GPa
71 GPa
Qenched
Fit
Exp
Spectrum # (data | fit)
2-Theta (degrees)
(b)
strain (%)
(c)
y=0.078+0.04731x
y=0.794+0.00655x
Twin-fault (%)
Pressure (GPa)

Figure 7

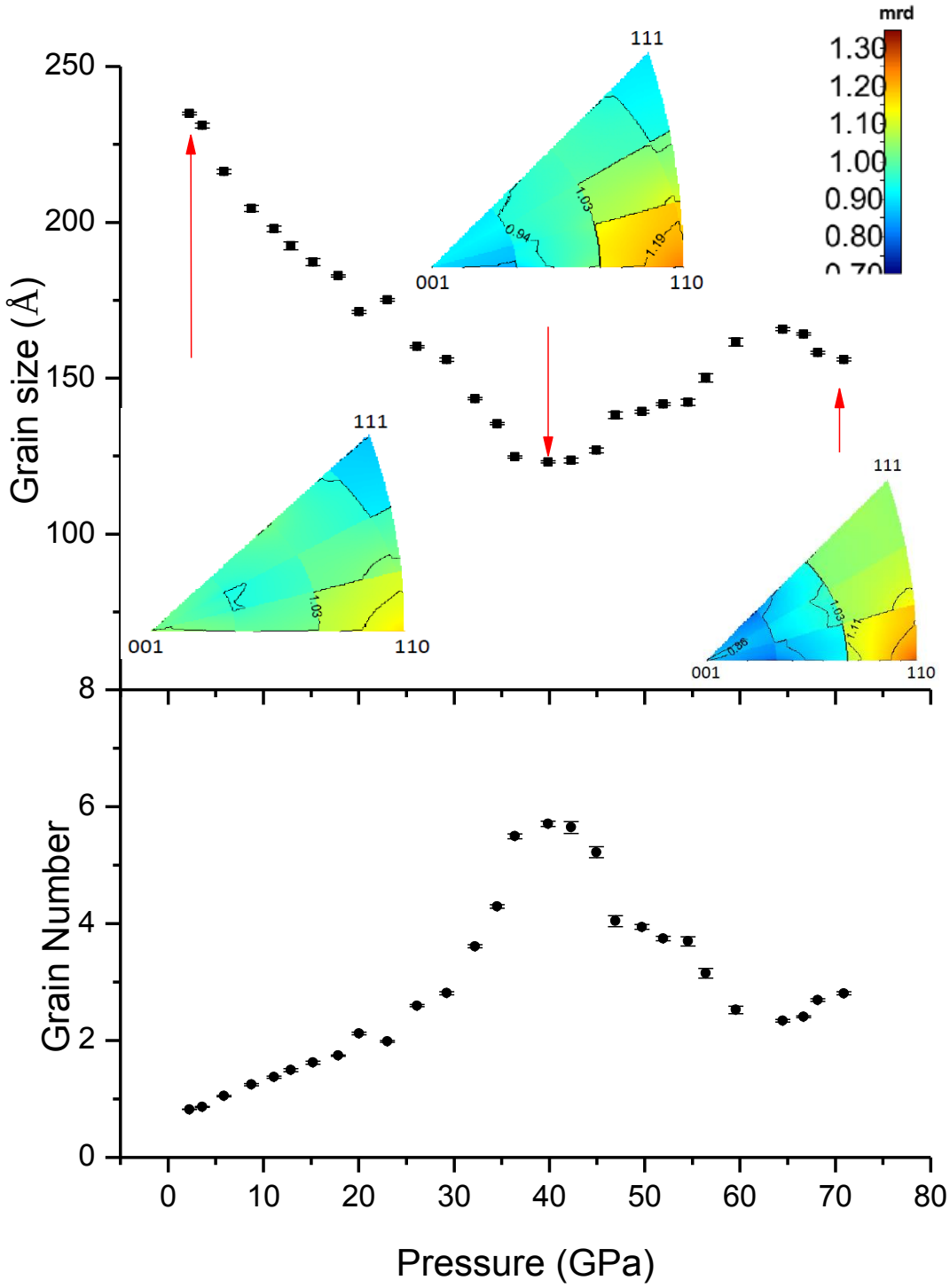
mrd
1.30
1.20
1.10
1.00
0.90
0.80
111
001
110
1.03
0.94
1.19
111
001
110
1.03
111
001
110
0.86
1.03
1.11
Grain size (Å)
250
200
150
100
8
Grain Number
6
4
2
0
0
10
20
30
40
50
60
70
80
Pressure (GPa)